

https://doi.org/10.1070/QEL16278

Effective dielectric function of TiO_2 nanoparticles under laser pumping in the fundamental absorption band

D.A. Zimnyakov, S.A. Yuvchenko

Abstract. **A nonlinear optical response of TiO_2 nanoparticles under pumping by 355-nm laser radiation is experimentally investigated. Using the data obtained by *z*-scanning with simultaneous measurement of the scattering intensity, the effective permittivity of particles is reconstructed as a function of the pump intensity. It is found that graphical mapping of the relationship between the real and imaginary parts of the permittivity can be obtained using an affine transformation of a similar map of the frequency-dependent dielectric function for the Lorentz model. It is shown that an increase in the pump intensity should lead to a red shift of the absorption maximum of nanoparticles and a rise in the plasma frequency, which is estimated (using a single-oscillator Lorenz model) from the obtained values of the real and imaginary parts of the effective permittivity for the probe radiation wavelength in use.**

Keywords: *nonlinear scattering, nonlinear absorption, dielectric function, titanium dioxide.*

1. Introduction

Study of the resonance and nonlinear optical effects upon interaction of light with nanostructures has become one of the key fields of research in optics in the last two decades. One of these effects is the excitation of localised surface plasmon resonances (LSPRs) [1–3]. Recently, a number of materials are considered as an alternative to noble metals, which are traditionally used in nanoplasmonics; examples are narrow-gap semiconductors and quasi-metals [4]. We should also note the works devoted to the synthesis and analysis of the properties of metamaterials in the optical range [5, 6].

In terms of optical electrodynamics, the key factor determining the possibility of such effects is the existence of some specific features of the frequency dependence of the permittivity. These features include the presence of spectral regions in which the real part of the dielectric function takes negative values. The analysis of the peculiarities of the dielectric function in the optical range is one of the key factors in estimation of the applicability of a particular medium in nanophotonics. The development of methods for controlling the dielectric function of a material by applying low-frequency or optical fields is also of interest.

In this paper, we report the results of studying the behaviour of the dielectric function of TiO_2 in the nanophase (in the form of spheroidal particles 40 nm in diameter) under pulsed 355-nm laser pumping. Titanium dioxide (wide-gap semiconductor with a band gap of about 3.2 eV) is of interest for various applications in modern optics due to the high scattering efficiency of TiO_2 particles in the visible and near-UV regions (an example is the development of random lasers [7]). Due to the negative values of the real part of the dielectric function of TiO_2 for $\lambda \leqslant 300$ nm, LSPRs occur in nanoparticles. These resonances manifest themselves as peaks in the extinction and depolarisation spectra of nanoplates and nanoribbons based on TiO_2 derivatives [8–10]. Note that, for the pump wavelength λ_p in use, the photon energy ($\sim$3.5 eV) exceeds the TiO_2 band gap, and the absorption peak ($\lambda_{max} \approx 285$ nm) is blue-shifted with respect to λ_p.

2. Experimental technique and results

We investigated water suspensions of TiO_2 nanoparticles with an average diameter of 40 nm (US Research Nanomaterials, US 3493). The mass fraction of particles was 10^{-3}; this value provided (at a cell thickness of 10 mm) a single interaction regime for the laser radiation and the medium. A schematic of the experimental setup is shown in Fig. 1. The *z*-scan method [11] with a closed aperture and simultaneous measurement of the radiation intensity scattered at an angle of 90° was used. This method implies measurement of the optical transmission of a sample, which is moved along the axis of a focused laser beam, as a function of the distance between the sample and

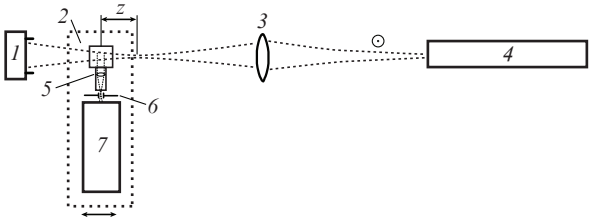

Figure 1. Schematic of the experimental setup: (*1*) Gentec Maestro Q12MF1 energy meter; (*2*) cell with a sample; (*3*) quartz lens; (*4*) laser; (*5*) lens block for focusing scattered radiation onto the spectrometer slit; (*6*) spectrometer input slit; (*7*) QE65000 spectrometer (Ocean Optics); *z* is the distance from the cell centre to the beam waist; symbol ⊙ indicates the beam polarisation direction. Elements (*2*, *5*, *6*, *7*) are mounted on a translation stage.

D.A. Zimnyakov Yuri Gagarin State Technical University of Saratov, ul. Politekhnicheskaya 77, 410054 Saratov, Russia; Institute of Problems of Precise Mechanics and Control, Russian Academy of Sciences, ul. Rabochaya 24, 410028 Saratov, Russia; e-mail: zimnykov@mail.ru;
S.A. Yuvchenko Yuri Gagarin State Technical University of Saratov, ul. Politekhnicheskaya 77, 410054 Saratov, Russia

Received 18 December 2016; revision received 19 March 2017
Kvantovaya Elektronika **47** (6) 547–552 (2017)
Translated by Yu.P. Sin'kov

beam waist. The probe radiation intensity is maximal in the waist; this maximum value is determined by the laser pulse energy, pulse duration, and the beam diameter in the waist. In our case, the optical transmission is measured simultaneously with the measurement of the Rayleigh scattering intensity from nanoparticles at an angle of 90° with respect to the probe beam direction. To provide the maximum scattering efficiency, the probe-beam electric field should be oriented perpendicular to the scattering plane, in which the wave vectors of the probe beam and recorded scattered radiation lie.

The radiation source was a pulsed frequency-tripling YAG : Nd laser of LS-2134 type (Lotis TII). The pulse energy was 2 mJ, the pulse duration was $\tau_{pls} = 10$ ns, and the pulse repetition rate was 15 Hz. The beam was focused by a quartz lens with $F = 110$ mm. The light transmitted through the cell was recorded by a Gentec Maestro energy meter with a Gentec Q12MF1 sensor. The cell with a sample was placed on a Standa 8MT167-100 motorised translation stage, which provided the cell displacement jointly with the system for measuring the Rayleigh scattering intensity [a QE65000 spectrometer (Ocean Optics) with a fixed input slit 50 μm wide and a lens block for focusing scattered light onto the slit]. The lens block was a 74DA collimator (Ocean Optics), connected directly to the input connector of the spectrometer. In this configuration, the collimator collects light into a narrow solid angle and focuses it onto the input slit.

Before starting the measurements, the system was calibrated in order to estimate the average pump radiation intensity I_p as a function of the cell centre position with respect to the beam waist. The calibration was performed using transverse beam scanning in different cross sections by a half-plane screen, with simultaneous measurement of transmitted-pulse energy. The data obtained were used to reconstruct the intensity distributions in different cross sections on the assumption that they have a Gaussian shape; the thus constructed three-dimensional distribution was used to calculate the I_p values averaged over the cell volume (Fig. 2).

The samples were exposed to light for a short time in our experiments. For each cell position on the beam z axis, the average laser radiation intensities transmitted through the cell and scattered from it were determined for a group of five pulses, after which, before displacing the cell to a new position, the exhausted portion of suspension was replaced with a fresh one. This was done to exclude the influence of the photoinduced change in the electronic structure of particles (in particular, their photobleaching) on the measurement results. Preliminary experiments on laser pumping of the water suspensions under study with different exposure times showed that the dependences of the light intensity transmitted through the sample on I_p are radically different for short (shorter than 0.4 s) and long (longer than 2 s) exposures. In particular, at short exposures, one observes a decrease in the optical transmission of the samples and an increase in the scattered light intensity with an increase in I_p. In contrast, long exposures cause a passage to the laser radiation–medium interaction regime, which is characterised by an increase in the optical transmission with an increase in the pump intensity. The samples probed in this regime at high pump intensities directly after the experiment exhibit a much higher optical transmission in the linear regime (at low pump intensities) in comparison with the initial samples before the experiment. In our opinion, this photobleaching can be related to the absorption saturation due to the ground-state depletion in the probed system [9] when photoelectrons are captured by traps (surface defects of the crystal structure of TiO_2 nanoparticles). The relaxation of the optical transmission to the initial level after the laser irradiation occurs for a rather long time (on the order of several tens of seconds); it may be due to a great extent to the diffusive and convective processes of particle mixing in the cell. In any case, the study of the interaction kinetics of the probe radiation and the analysed systems under long-term exposure, being of independent interest, is beyond the scope of this study. In this context, we chose experimental conditions providing maximal suppression of the effects of the aforementioned photobleaching and particle mixing in the cell (i.e., exposure times that do not exceed 0.4 s and correspond to a series of five laser pulses).

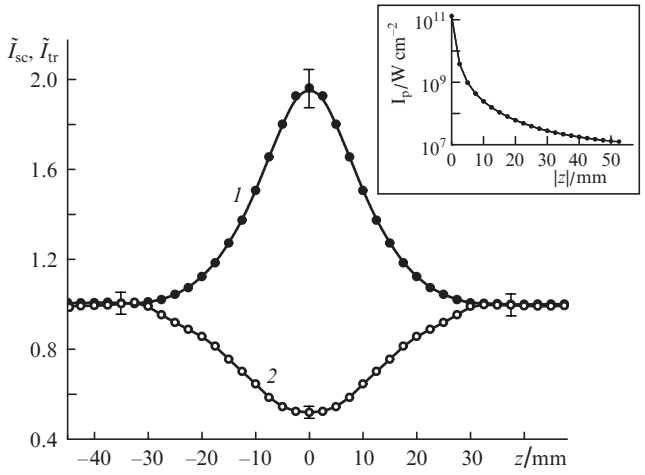

Figure 2. Dependences of the normalised intensities of (*1*) the scattered light and (*2*) the light transmitted through the sample on the pump intensity, which was determined for each value using the dependence $I_p(|z|)$ presented in the inset.

Figure 2 shows the normalised averaged intensities of the transmitted $\tilde{I}_{tr}(I_p)$ and scattered $\tilde{I}_{sc}(I_p)$ beams (the normalisation was performed to the intensity corresponding to the cell position at a large distance from the beam waist). Thus, $\tilde{I}_{tr}(I_p) = I_{tr}(I_p)/I_{tr}(I_p \to 0)$ and, correspondingly, $\tilde{I}_{sc}(I_p) = I_{sc}(I_p) \times [I_{sc}(I_p \to 0)]^{-1}$, where I_{sc} and I_{tr} are, respectively, the measured intensities of the scattered radiation and the radiation transmitted through the cell; the condition $I_p \to 0$ corresponds to low pump intensities, which do not affect the optical characteristics of the systems under study (linear interaction regime, which was implemented at cell displacements from the waist along the z axis by distances above 35 mm). The confidence intervals in the plots correspond to a significance level of 0.9.

3. Discussion of the experimental results

The data obtained were interpreted using an approach different from the conventional analysis of z-scan data, which is based on the estimation of the susceptibilities of different orders [11]. For particles pumped with a specified intensity I_p, we considered the effective value of the dielectric function $\tilde{\varepsilon}(I_p) = \tilde{\varepsilon}'(I_p) + i\tilde{\varepsilon}''(I_p)$, normalised to the permittivity of the medium containing particles. The effective permittivity of the pumped particles is equal to the permittivity of 'test' particles (having the same volume and shape and made of some material) in the absence of laser pumping. The mean scattering and absorption cross sections of the probed and 'test' spheroidal

particles are equal and determined {see [12], Chapter 12, expression (12.34)} as

$$\langle\sigma_{sc}(I_p)\rangle = \frac{k^4 v^2}{18\pi}\left|\tilde{\varepsilon}(I_p)-1\right|^2\left\{\frac{27}{\left[\tilde{\varepsilon}'(I_p)+2\right]^2+\tilde{\varepsilon}''^2(I_p)}\right\},$$
$$\langle\sigma_{abs}(I_p)\rangle = \frac{kv}{3}\left\{\frac{27}{\left[\tilde{\varepsilon}'(I_p)+2\right]^2+\tilde{\varepsilon}''^2(I_p)}\right\}\tilde{\varepsilon}''(I_p). \quad (1)$$

Here, k is the wave number of radiation in the matrix medium and v is the average particle volume. Expressions (1) characterise the fundamental features of the interaction of electromagnetic radiation with particles that are small in comparison with the radiation wavelength. These features include the directly proportional dependence of the absorption cross section on the particle volume and the inversely proportional dependence of this parameter on the probe light wavelength. At the same time, the scattering cross section is proportional to the squared volume and inversely proportional to the fourth power of wavelength (Rayleigh scattering). Note also that, due to the similarity of the dependences of scattering and absorption cross sections on the particle volume and wavelength, the absorption cross section exceeds the scattering cross section at a nonzero imaginary part of the permittivity for particles with diameters smaller than $k^{-1}\times\sqrt[3]{36\tilde{\varepsilon}''/\left|\tilde{\varepsilon}'-1\right|^2}$. Another fundamental feature of the interaction of light with spherical nanoparticles, which follows from expressions (1), is the resonance amplification of scattering and absorption, which occurs when the real part of the permittivity satisfies the Frohlich condition: $\tilde{\varepsilon}'=-2$. The efficiency of this resonance amplification is limited by the imaginary part of the permittivity and decreases when the latter increases.

The radiation intensity $I_{sc}(I_p)$ scattered by a disordered ensemble of particles is proportional to $\langle\sigma_{sc}(I_p)\rangle NI_p$, while the transmitted radiation intensity $I_{tr}(I_p)$ can be presented as

$$I_p\exp\{-\rho d[\langle\sigma_{sc}(I_p)\rangle+\langle\sigma_{abs}(I_p)\rangle]\},$$

where N is the number of particles in the probed scattering volume, ρ is the particle concentration, and d is the cell thickness. We take into account that the cell displacement along the probe beam axis changes the beam cross-sectional area S in the detection zone of scattered radiation, while the zone size along the beam direction remains the same. The number of particles in the detection zone is proportional to the beam cross-sectional area and the particle concentration ($N\sim S\rho$), while the pump intensity is proportional to the laser pulse energy and inversely proportional to the beam cross-sectional area and pulse duration; i.e., $I_{sc}(I_p)\sim\langle\sigma_{sc}(I_p)\rangle\rho(E/\tau_{pls})$. Thus, at fixed values of the particle concentration and laser pulse energy and duration, the normalised scattered radiation intensity $\tilde{I}_{sc}(I_p)=I_{sc}(I_p)/I_{sc}(I_p^{lin})$ is equal to the ratio $\langle\sigma_{sc}(I_p)\rangle/\langle\sigma_{sc}(I_p^{lin})\rangle$. Therefore, the scattered radiation intensity at small I_p values (linear mode) should be constant, and its variations near the waist are controlled by only the dependence of the scattering cross section of particles on the pump intensity. In accordance with (1), at constant values of the particle volume and probe radiation wave number, this dependence is only determined by the variations in the particle permittivity with a change in the pump intensity. This conclusion is confirmed by the observed behaviour of the normalised scattered radiation intensity $\tilde{I}_{sc}(I_p)$: it is constant ($\tilde{I}_{sc}(I_p)=1$) at low pump intensities (at $|z|\geqslant 35$ mm) but significantly increases in the waist region (see Fig. 2). Using expression (1), one can present the normalised scattered radiation intensity in the form

$$\tilde{I}_{sc}(I_p)=\frac{\langle\sigma_{sc}(I_p)\rangle}{\langle\sigma_{sc}(I_p^{lin})\rangle}=\frac{\left[\tilde{\varepsilon}'(I_p)-1\right]^2+\tilde{\varepsilon}''^2(I_p)}{\left[\tilde{\varepsilon}'(0)-1\right]^2+\tilde{\varepsilon}''^2(0)}\times\frac{\left[\tilde{\varepsilon}'(0)+2\right]^2+\tilde{\varepsilon}''^2(0)}{\left[\tilde{\varepsilon}'(I_p)+2\right]^2+\tilde{\varepsilon}''^2(I_p)}, \quad (2)$$

where $\tilde{\varepsilon}'(0)$ and $\tilde{\varepsilon}''(0)$ correspond to small $I_p=I_p^{lin}$ (linear scattering and absorption). To continue the analysis, we assumed that $\tilde{\varepsilon}'(0)=9.67$ and $\tilde{\varepsilon}''(0)=2.19$ (these values were calculated for $\lambda=355$ nm from the optical constants n (refractive index) and k (absorption coefficient) [12] for bulk titanium dioxide [13]) and introduced the following parameter:

$$\Phi(I_p)=\tilde{I}_{sc}(I_p)\frac{\left[\tilde{\varepsilon}'(0)-1\right]^2+\tilde{\varepsilon}''^2(0)}{\left[\tilde{\varepsilon}'(0)+2\right]^2+\tilde{\varepsilon}''^2(0)}.$$

The value of $\Phi(I_p^{lin})$ in the linear region, where $\tilde{I}_{sc}(I_p)=1$, is approximately found to be 0.567.

Similarly, let us consider the ratio of the transmitted light intensity to the pump intensity: $I_{tr}(I_p)/I_p$. This ratio in the linear region (at low pump intensities $I_p=I_p^{lin}$) was measured to be 0.223. Using the expression $\ln[I_p/I_{tr}(I_p)]=d\rho[\langle\sigma_{sc}(I_p)\rangle+\langle\sigma_{abs}(I_p)\rangle]$, we will analyse the ratio

$$\frac{\ln[I_p/I_{tr}(I_p)]}{\ln[(I_p^{lin})/I_{tr}(I_p^{lin})]}=\frac{\langle\sigma_{sc}(I_p)\rangle+\langle\sigma_{abs}(I_p)\rangle}{\langle\sigma_{sc}(I_p^{lin})\rangle+\langle\sigma_{abs}(I_p^{lin})\rangle}.$$

Here, I_p^{lin} is used to indicate the pump intensities corresponding to 'linear' z-scan regions ($|z|\geqslant 35$ mm). Having transformed this expression, with allowance for the fact that the measured sample transmittance at a specified pump intensity I_p can be presented as

$$\frac{I_{tr}(I_p)}{I_p}=\frac{\tilde{I}_{tr}(I_p)[I_{tr}(I_p^{lin})]}{I_p^{lin}},$$

we arrive at

$$\frac{\ln\{(I_p^{lin})/[\tilde{I}_{tr}(I_p)I_{tr}(I_p^{lin})]\}}{\ln[(I_p^{lin})/I_{tr}(I_p^{lin})]}=\frac{\langle\sigma_{sc}(I_p)\rangle}{\langle\sigma_{sc}(I_p^{lin})\rangle}\frac{1+\langle\sigma_{abs}(I_p)\rangle/\langle\sigma_{sc}(I_p)\rangle}{1+\langle\sigma_{abs}(I_p^{lin})\rangle/\langle\sigma_{sc}(I_p^{lin})\rangle}.$$

As was shown above, the $\langle\sigma_{sc}(I_p)\rangle/\langle\sigma_{sc}(I_p^{lin})\rangle$ ratio is equal in our case to the normalised scattered radiation intensity $\tilde{I}_{sc}(I_p)$, while the $\langle\sigma_{abs}(I_p)\rangle/\langle\sigma_{sc}(I_p)\rangle$ ratio can be written [with allowance for expression (1)] as

$$\frac{\langle\sigma_{abs}(I_p)\rangle}{\langle\sigma_{sc}(I_p)\rangle}=\frac{6\pi}{k^3v}\frac{\tilde{\varepsilon}''(I_p)}{\left[\tilde{\varepsilon}'^2(I_p)-1\right]^2+\tilde{\varepsilon}''^2(I_p)}.$$

Using the values of the mean diameter of TiO_2 particles and the probe radiation wave number in water, the parameter $6\pi/k^3v$ for the medium under study is found to be about 38.38, while the $\langle\sigma_{abs}(I_p^{lin})\rangle/\langle\sigma_{sc}(I_p^{lin})\rangle$ ratio is determined [using the above-reported values of $\tilde{\varepsilon}'(0)$ and $\tilde{\varepsilon}''(0)$] to be 1.051.

Thus, with allowance for the specific numerical values of the parameters of the system under study and the probe radiation, one can derive the following expression, establishing a relationship between the measured normalised values of

transmitted and scattered radiation intensities (Fig. 2) and the $\tilde{\varepsilon}'(I_p)$ and $\tilde{\varepsilon}''(I_p)$ values:

$$\frac{\ln[4.484/\tilde{I}_{tr}(I_p)]}{1.501\tilde{I}_{sc}(I_p)} \approx \frac{1}{2.051}\left\{1 + 38.38\frac{\tilde{\varepsilon}''(I_p)}{[\tilde{\varepsilon}'^2(I_p) - 1]^2 + \tilde{\varepsilon}''^2(I_p)}\right\}.$$

The term $\ln[4.484/\tilde{I}_{tr}(I_p)]$ and factor 1.501 correspond to $\ln\{(I_p^{lin})/[\tilde{I}_{tr}(I_p)I_{tr}(I_p^{lin})]\}$ and $\ln[(I_p^{lin})/I_{tr}(I_p^{lin})]$ at the experimentally found value $I_{tr}(I_p^{lin})/I_p^{lin} \approx 0.223$, and 2.051 is the numerical value of the expression $1 + \langle\sigma_{abs}(I_p^{lin})\rangle \times \langle\sigma_{sc}(I_p^{lin})\rangle^{-1}$. To simplify further analysis, we introduce the following parameter: $\Gamma(I_p) = 2.051\{\ln[4.484\tilde{I}_{tr}(I_p)]/[1.501\tilde{I}_{sc}(I_p)]\} - 1$.

Figure 3 shows the dependences $\Phi(I_p)$ and $\Gamma(I_p)$, obtained using the above-described procedure of modifying the scattering and damping data; the dependences were smoothed using *B*-spline interpolation. The confidence intervals correspond to a significance level of 0.9. The relationship between the parameters $\Phi(I_p)$ and $\Gamma(I_p)$ calculated from experimental data and the effective values $\tilde{\varepsilon}'(I_p)$ and $\tilde{\varepsilon}''(I_p)$ is set by the system

$$\Phi(I_p) \approx \frac{[\tilde{\varepsilon}'^2(I_p) - 1]^2 + \tilde{\varepsilon}''^2(I_p)}{[\tilde{\varepsilon}'^2(I_p) + 2]^2 + \tilde{\varepsilon}''^2(I_p)},$$

$$\Gamma(I_p) \approx 38.38\frac{\tilde{\varepsilon}''(I_p)}{[\tilde{\varepsilon}'^2(I_p) - 1]^2 + \tilde{\varepsilon}''^2(I_p)}. \qquad (3)$$

Note that the parameter $\tilde{\varepsilon}'(I_p)$ is smaller than unity for non-negative $\Phi(I_p) < 1$ values; at $\tilde{\varepsilon}'(I_p) = -0.5$, the parameter $\Phi(I_p) = 1.0$ and becomes larger than unity with a further decrease in the real part of the effective permittivity.

After reducing the equations of system (3) to the canonical form, it was solved numerically with respect to $\tilde{\varepsilon}'(I_p)$ and $\tilde{\varepsilon}''(I_p)$ using the Newton method for selective values $\Phi(I_p)$ and $\Gamma(I_p)$, indicated by markers in Fig. 3. The $\tilde{\varepsilon}'(0)$ and $\tilde{\varepsilon}''(0)$ values were chosen as initial ones. The thus obtained distributions of reconstructed values of the effective dielectric function $\tilde{\varepsilon}'' = f_{eff}(\tilde{\varepsilon}')$ in the $(\tilde{\varepsilon}', \tilde{\varepsilon}'')$ plane for the pump intensity range in use is presented in Fig. 4. Note that the function $\tilde{\varepsilon}'' = f_{eff}(\tilde{\varepsilon}')$ in the range of pump intensities from 5×10^6 to 1.08×10^{11} W cm^{-2} can be presented with a high degree of accuracy by a portion of an elliptical curve described by the equation

$$\left[\frac{\tilde{\varepsilon}'(I_p) + 4.0}{31.9}\right]^2 + \left[\frac{\tilde{\varepsilon}''(I_p) - 30.5}{31.6}\right]^2 = 1. \qquad (4)$$

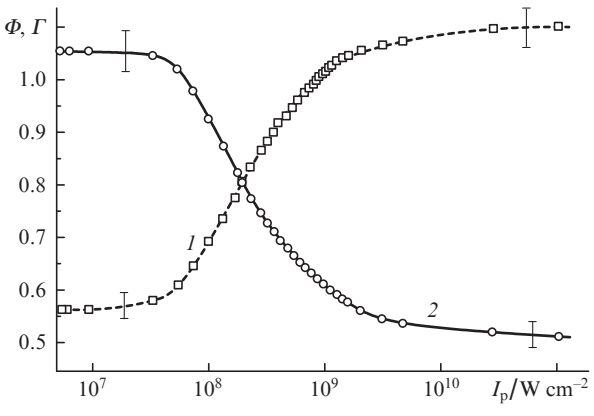

Figure 3. Dependences of (*1*) Φ and (*2*) Γ on the pump intensity.

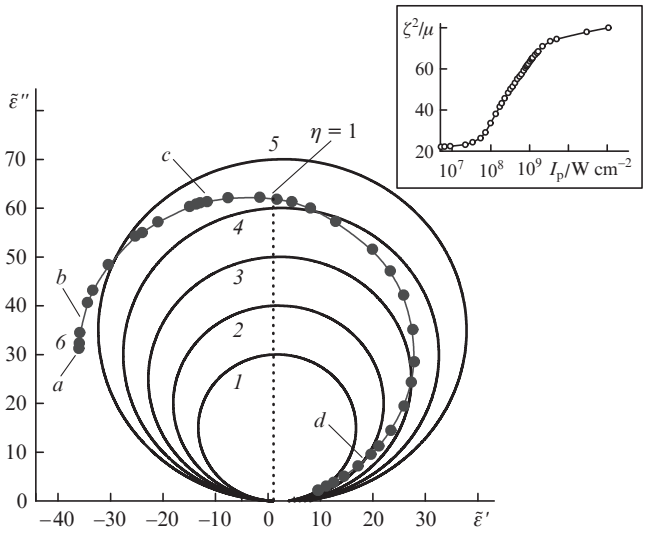

Figure 4. Functions (*1–5*) $\varepsilon'' = f_{mod}(\varepsilon')$ and (*6*) $\tilde{\varepsilon}'' = f_{eff}(\tilde{\varepsilon}')$ at ζ^2/μ = (*1*) 30, (*2*) 40, (*3*) 50, (*4*) 60, and (*5*) 70. The dotted line corresponds to $\tilde{\varepsilon}' = 1$. The letters *a–d* stand for I_p = (*a*) 1.08×10^{11}, (*b*) 1.0×10^{10}, (*c*) 1.0×10^9, and (*d*) 1.0×10^8 W cm^{-2}. The inset shows the dependence of the parameter ζ^2/μ on the pump intensity.

At the same time, the frequency dependences of the real and imaginary parts of the dielectric function of the system with resonance absorption are described in the simplest case within the single-oscillator Lorenz model, which satisfies the Kramers–Kronig relations [12]:

$$\tilde{\varepsilon}' = 1 + \frac{\zeta^2(1-\eta^2)}{(1-\eta^2)^2 + \mu^2\eta^2},$$

$$\tilde{\varepsilon}'' = \frac{\zeta\mu\eta}{(1-\eta^2)^2 + \mu^2\eta^2}. \qquad (5)$$

Here, η, ζ, and μ, are respectively, the electromagnetic-wave frequency ω, plasma frequency ω_p, and damping parameter γ, normalised to the resonance frequency ω_0. The ω_0 value is considered to be the resonance frequency of the model harmonic oscillators interacting with the electromagnetic wave. An ensemble of such noninteracting oscillators (atoms) imitates the medium under study within the classical Lorenz model, and the number of oscillators per unit volume determines the plasma frequency of this medium. For Lorentz systems with a not very large damping parameter γ (satisfying the condition $\gamma \ll \omega_0$), the maximum values of the absorption coefficient k and imaginary part of the permittivity, $\tilde{\varepsilon}''$, are obtained at frequencies close to the resonance one [12]. For bulk titanium dioxide and low probe radiation intensities, an analysis of the dependences $\tilde{\varepsilon}'(\omega)$ and $\tilde{\varepsilon}''(\omega)$, reconstructed from the refractive index and absorption coefficient spectra [13], makes it possible to estimate approximately the Lorentz model parameters: $\omega_0 \approx 6.24\times 10^{15}$ Hz, $\omega_p \approx 1.18\times 10^{16}$ Hz, $\gamma \approx 1.32\times 10^{15}$ Hz. The model fairly adequately describes the behaviour of the frequency dependences $\tilde{\varepsilon}'(\omega)$ and $\tilde{\varepsilon}''(\omega)$ reconstructed from the data on optical constants [8, 9].

Assuming the ζ and μ values to be fixed and considering the relationship between $\tilde{\varepsilon}'$ and $\tilde{\varepsilon}''$ in the range $0 \leqslant \eta \leqslant \infty$, one can show that the model functions $\tilde{\varepsilon}'' = f_{mod}(\tilde{\varepsilon}')$ for a Lorentz system can be presented with a high accuracy by open elliptical lines in the $(\tilde{\varepsilon}', \tilde{\varepsilon}'')$ plane at $\mu \leqslant 0.2$. The approximating elliptical lines are open due to the difference in the limiting

values $\tilde{\varepsilon}'_{\eta\to\infty}\to 1$ and $\tilde{\varepsilon}'_{\eta\to 0}\to 1+\zeta^2$ at $\tilde{\varepsilon}''=0$. The lengths of their axes, defined as $\tilde{\varepsilon}''_{\max}$ and $\tilde{\varepsilon}'_{\max}-\tilde{\varepsilon}'_{\min}$, are approximately equal (the eccentricity is close to zero) and amount to ζ^2/μ, whereas the positions of their centers are approximately determined by the coordinates $(1, \zeta^2/2\mu)$.

The behaviour of the dependences $\tilde{\varepsilon}''=f_{\text{eff}}(\tilde{\varepsilon}')$ and $\tilde{\varepsilon}''=f_{\text{mod}}(\tilde{\varepsilon}')$ suggests the existence of their affine similarity, allowing the possibility of mutual transformation $\eta(\omega),\zeta(\omega),\mu(\omega)\leftrightarrow\eta(I_p),\zeta(I_p),\mu(I_p)$, which is reduced to the expansion/contraction and shift of mapping lines. Any pair of $\tilde{\varepsilon}', \tilde{\varepsilon}''$ values in the $\tilde{\varepsilon}''=f_{\text{eff}}(\tilde{\varepsilon}')$ plot in Fig. 4 can unambiguously be presented by a certain point of the parametric dependence $\tilde{\varepsilon}''=f_{\text{mod}}(\tilde{\varepsilon}')$, derived from system (5) with the corresponding choice of the parameters ζ^2/μ and η. It follows from the correspondence between system (5) and the Kramers–Kronig relations that the function $\tilde{\varepsilon}''=f_{\text{eff}}(\tilde{\varepsilon}')$, obtained from experimental data, also satisfies these relations. It can be seen in Fig. 4 that the ζ^2/μ value, at which the system

$$\tilde{\varepsilon}''=f_{\text{eff}}(\tilde{\varepsilon}'),$$

$$\tilde{\varepsilon}''=f_{\text{mod}}(\tilde{\varepsilon}')$$

has a solution at a specified pump intensity I_p, increases with an increase in I_p. The inset in Fig. 4 shows the dependence of ζ^2/μ on I_p for the nanoparticles under study, which is characterised by significant changes in this parameter in the range of pump intensities from 4.4×10^7 to 2.2×10^9 W cm^{-2} and saturation with a further increase in I_p.

Note that the increase in ζ^2/μ is due to the changes in the resonance frequency ω_0 of the system, the plasma frequency ω_p, and presumably the damping parameter γ. In particular, at $I_p\approx 8.8\times10^8$ W cm^{-2}, $\tilde{\varepsilon}'\approx 1$; this approximate equality corresponds to $\eta\approx 1$ ($\omega\approx\omega_0$) (the dotted line in Fig. 4). Taking into account that the maximum value of the absorption coefficient of the system is obtained at a frequency close to the resonance frequency for the corresponding model Lorentz medium, one can suggest that the absorption peak of particles is red-shifted (approximately from 284 to 355 nm) with a change in I_p from 0 to 8.8×10^8 W cm^{-2}. The increase in ζ^2/μ is also due to the increase in the parameter ω_p^2/γ. For example, for the pump regime corresponding to the dotted line in Fig. 4, the $(\omega_p^2/\gamma)_{\text{nl}}/(\omega_p^2/\gamma)_{\text{l}}$ ratio is estimated to be about 1.65 (the subscript nl corresponds to the nonlinear interaction regime, and the subscript l stands for the linear regime at small I_p values).

The real part $\tilde{\varepsilon}_{\text{eff}}$ of pumped particles takes negative values at $I_p\geqslant 9.2\times10^8$ W cm^{-2}. Resonance excitation of collective oscillations of charge carriers (LSPR) may occur at $\tilde{\varepsilon}'=-2$ (the Frohlich condition for spherical nanoparticles); however, this excitation is suppressed because of the large value of the imaginary part of $\tilde{\varepsilon}_{\text{eff}}$.

Note that, at high pump intensities, an additional factor that may affect the interaction of the probe radiation with TiO_2 nanoparticles is the formation of vapour nanobubbles around the particles heated by laser pulses. This process may also significantly affect the scattering and absorption cross sections of the particles, manifesting itself in the experimentally determined dependences of $\tilde{I}_{\text{sc}}$ and $\tilde{I}_{\text{tr}}$ on the pump intensity I_p. This effect in the case under consideration was analysed by estimating the scattering cross sections for the 'spherical TiO_2 core–vapour shell' complexes in dependence of the shell thickness h. The real and imaginary parts of the shell dielectric function were taken to be $\tilde{\varepsilon}'=1.0$ and $\tilde{\varepsilon}''=0$. The measured $\tilde{I}_{\text{sc}}$ values are proportional to the scattering cross section of hypothetical complexes at a specified pump intensity; correspondingly, the effect of vapour shell formation should directly manifest itself in the dependence $\tilde{I}_{\text{sc}}(I_p)$. The scattering cross sections of complexes with different h values were estimated using the on-line calculator of the optical characteristics of hybrid nanoparticles [14], which is based on the model of light scattering by a sphere in a shell [12]. The calculation results are presented in Fig. 5 for three TiO_2 core diameters close to the average diameter of the nanoparticles used in the experiment. Note the highly nonmonotonic behaviour of the scattering cross section of the complexes, which manifests itself in the sharp drop of the scattering cross section almost to zero with an increase in the shell thickness from zero to some critical value h_{cr}, with a subsequent sharp rise at $h>h_{\text{cr}}$. Qualitatively, the existence of a minimum scattering cross section at $h=h_{\text{cr}}$ can be interpreted as a manifestation of the destructive interference upon interaction of the internal fields of the shell and core of the complex, excited by the incident-wave field. The minimum scattering cross section of the complexes is obtained at a certain relation between the diameter of the core, thickness of the shell, and their refractive indices; however, a detailed analysis of this issue is beyond the scope of this study. The absorption cross section of the complexes changes little: it slightly decreases with a decrease in the scattering cross section and increases at $h>h_{\text{cr}}$.

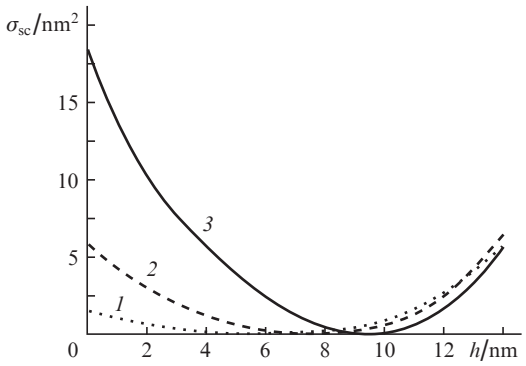

Figure 5. Simulated dependences of the scattering cross section for 'spherical TiO_2 core–vapour shell' complexes in water on the vapour-shell thickness. The TiO_2 core diameters are (*1*) 20, (*2*) 25, and (*3*) 30 nm; the light wavelength is 355 nm.

Having compared the simulation results presented in Fig. 5 with the experimental dependence $\tilde{I}_{\text{sc}}(I_p)$ (see Fig. 2), one can conclude that the formation of nanobubbles does not significantly affect the interaction of the probe radiation with nanoparticles, at least up to the maximum pump intensities implemented in the experiment. This conclusion stems from the fact that the formation of a vapour shell and its growth to certain limits with an increase in I_p, which significantly reduce the scattering efficiency, should manifest themselves in a nonmonotonic behaviour of the dependence $\tilde{I}_{\text{sc}}(I_p)$ or at least in the existence of peculiarities (such as a plateau or an inflection point) in it at pump intensities below the maximum value. However, these features were not observed experimentally (Fig. 2). This may be due to the relatively low conversion efficiency of absorbed optical power into heat for TiO_2 nanoparticles in comparison with nanoparticles of other types (e.g., metal or carbon ones).

4. Conclusions

The very good correspondence between the empirical function $\tilde{\varepsilon}'' = f_{\text{eff}}(\tilde{\varepsilon}')$ (dependent on I_p) for TiO_2 nanoparticles and a simple analytical form within the Lorenz model appears to be unexpected. However, it was previously noted that the Lorentz model can be used for adequate description of the peculiarities of extinction spectra caused by resonance excitations of charge-carrier oscillations in nanoplates of TiO_2 derivatives [8, 9]. In addition, the system was pumped near the fundamental absorption edge with relatively low intensities and short exposure times, at which the effects causing significant changes in the electronic structure of particles (for example, depletion of the ground state) are absent or do not affect much their optical properties. Within the classical concepts about the interaction of optical electromagnetic fields with matter, specific features have been established in the behaviour of the effective dielectric function of TiO_2 nanoparticles (derived from experimental data): increase in the imaginary part with an increase in the pump intensity to a certain limit and a subsequent drop with a further increase in I_p, as well as a decrease in the real part up to large (in magnitude) negative values. This behaviour is qualitatively similar to that of the frequency dependences of the real and imaginary parts of the dielectric function of bulk titanium dioxide [13] with an increase in frequency at low fixed probe intensities [8]; it is caused by the increase in the charge-carrier concentration in the conduction band. An analysis of the data obtained suggests that the absorption peak of the system under study should be red-shifted with an increase in the pump intensity.

We believe the results of this study to be of interest for developing the methods of optical control of the dielectric and optical properties of dispersed nanomaterials.

Acknowledgements. This work was supported by the Russian Science Foundation (Grant No. 16-19-10455) in the development and implementation of the experimental technique and by the Ministry of Education and Science of the Russian Federation (Grant No. 3.7567.2017) in the theoretical analysis of the data.

References

1. Barnes W.L., Dereux A., Ebbesen T.W. *Nature*, **424**, 6950 (2003).
2. Locharoenrat K., Sano H., Mizutani G. *Sci. Tech. Adv. Mater*., **109**, 1492 (2007).
3. Shu Z., Xiaodong P. *ACS Nano*, **9**, 378 (2015).
4. Naik G.V., Shalaev V.M., Boltasseva A. *Adv. Mater*., **25**, 24 (2013).
5. Stockman M.I. *Opt. Express*, **19**, 22029 (2011).
6. Shalaev V.M. *Nat. Photonics*, **1**, 41 (2007).
7. Lawandy N.M., Balachandran R.M., Gomes A.S., Sauvain E. *Nature*, **368**, 6470 (1994).
8. Zimnyakov D.A., Gorokhovsky A.V., Tret'yachenko E.V., Ushakova O.V., Isaeva E.A., Isaeva A.A. *Opt. Mater*., **34**, 11 (2012).
9. Zimnyakov D.A., Ushakova O.V., Gorokhovsky A.V., Tretyachenko E.V., Isaeva E.A., Isaeva A.A., Pravdin A.B. *Appl. Opt*., **51**, 3675 (2012).
10. Zimnyakov D.A., Zdrajevsky R.A., Yuvchenko S.A., Ushakova O.V., Angelsky O.V., Yermolenko S.B. *J. Quant. Spectrosc. Radiat. Transfer*, **152**, 37 (2015).
11. Sheik-Bahae M., Said A.A., Wei T.-H., Hagan D.J., Van Stryland E.W. *IEEE J. Quantum Electron*., **26**, 760 (1990).
12. Bohren C.F., Huffman D.R. *Absorption and Scattering of Light by Small Particles* (New York: Wiley, 1983; Moscow: Mir, 1986).
13. http://www.ioffe.ru/SVA/NSM/nk/Oxides/Gif/tio2b.gif.
14. https://nanocomposix.com/pages/tools.